Prospects for continuous-wave molecular modulation in Raman-active microresonators

JOSHUA T. KARPEL,[*] [iD] DAVID C. GOLD, AND DENIZ D. YAVUZ

Department of Physics, 1150 University Avenue, University of Wisconsin at Madison, Madison, WI 53706, USA
[*]*karpel@wisc.edu*

Abstract: We propose the extension of existing molecular modulation techniques for continuous-wave optical modulation to Raman-active microresonators. Intense pump and Stokes modes inside a microresonator prepare a high coherence of the Raman transition between two ro-vibrational states. With the coherence prepared, any laser in the optical region can be coupled to the microresonator and be modulated. We perform numerical simulations which predict that these "microresonator-based molecular modulators" could have modulation efficiencies on the order of 1% at 10 THz-scale frequencies for any optical wavelength.

1. Introduction

Optical modulators are powerful tools that have found a wide variety of uses, ranging from encoding information to synthesizing ultrafast waveforms. Acousto-optical and electro-optical modulators (AOMs and EOMs) provide frequency shifts limited to the electrical frequencies that drive them, with a maximum of a few hundred GHz. Although new techniques continue to incrementally improve electrically-driven modulators [1–5], there is little prospect for pushing them to significantly higher modulation frequencies. Optical modulators with THz-scale modulation frequencies need to be driven by optical processes.

Over the past decade our group created a 90 THz continuous-wave (CW) optical modulator based on a technique called molecular modulation, a kind of driven four-wave mixing based on CW Raman lasing [6–15]. Molecular modulation was originally developed using pulsed pump lasers [16–27], but these systems suffer from large linewidths and low repetition rates [28]. Using CW driving beams for our modulator avoided these problems, but required the use of an optical cavity to reach the high intensities necessary for molecular modulation to occur. Using a large gas-filled cavity ultimately limited the usefulness of the modulator due to its complexity of operation and sensitivity to mechanical and thermal fluctuations, all of which negatively impacted the steady-state modulation efficiency ϵ.

In this work we propose the extension of CW molecular modulation to solid-state Raman-active microresonators and discuss the prospective characteristics of such a device, which we call a Microresonator-based Molecular Modulator (MMM). We also present numerical simulations that indicate that an MMM based on a silica microsphere could achieve a frequency shift of ~ 12 THz with modulation efficiencies of $\epsilon \approx 1\%$ at any optical wavelength.

Microresonator modes have small volumes and high quality factors over a wide range of wavelengths, which make them ideal platforms for building nonlinear optical devices [29,30]. For example, Grudinin et al. demonstrated an ultra-low-threshold Raman laser in a CaF_2 microresonator which required just 15 μW of launched pump power [31,32]. Other groups have used microresonators to create high-quality stabilized optical frequency combs or explore more exotic nonlinear behavior such as soliton formation [33–35]. As an added benefit, the smaller overall system size and better mechanical and thermal stability offered by microresonators will help mitigate the issues that limited the efficiency of our previous device. Microresonators could also be integrated into complex optical systems much more readily.

Figure 1 shows a cartoon of the specific kind of proposed MMM we characterize in this work. A pump laser is evanescently coupled to one of the whispering gallery modes of a silica microsphere using a tapered fiber [36]. This "pump mode" builds up to high intensity. The pump mode then generates a high-intensity Stokes mode through stimulated Raman scattering (SRS). Once the pump and Stokes modes have both built up to high intensities, molecular modulation can occur: a separate low-power "mixing" beam is coupled to the resonator and is modulated via driven four-wave mixing to produce light at the "target" frequency.
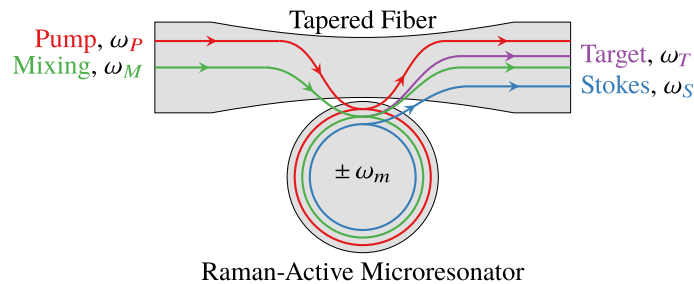

Fig. 1. A cartoon of our molecular modulation scheme implemented using a microsphere made of Raman-active material with frequency shift ω_m coupled to a tapered fiber. The launched pump beam at frequency ω_P drives a Stokes mode at frequency $\omega_S = \omega_P - \omega_m$ via Raman lasing. Then a launched "mixing" beam at frequency ω_M is modulated by the intense pump and Stokes modes via four-wave mixing to produce light at the "target" frequency $\omega_T = \omega_M + \omega_m$.

2. Theoretical modeling

To characterize the theoretical performance of MMMs we have derived a model of the four-wave mixing process in an arbitrary resonator. Typically, models of this process either do not perform a spatial decomposition at all (leading to the "sideband model") [37,38], or assume the well-known regular mode structure of a Fabry-Perot cavity [7,39,40]. In contrast, we decompose the electric field into the spatial modes of a generalized resonator as well as in time. We combine this description with models of the underlying quantum mechanics and of how light couples to the resonator (see [36,41,42]) to create an end-to-end, time-dependent model of the modulator.

The primary advantage of this model is that it makes no assumptions about the mode structure of the resonator or which inter-mode couplings might be more important than others. Instead, these relationships will arise emergently from the model, as they would in a real experiment. As we will see, this turns out to be critically important to understanding the behavior of the MMM.

An additional advantage of our model is that it includes all of the time-dependent behavior of the resonator (i.e., it is not solely concerned with steady-state behavior). We can use this to look at, for example, how long it takes the mode energies to reach steady-state after the pump laser turns on. Knowing that timescale will be critical for building optical modulators that can interoperate with other devices. A delay of several microseconds before the output power stabilizes could be important for both downstream and upstream devices. We plan to explore this aspect of the model in future work.

The full derivation of the model is too long to be included here, but we will briefly sketch it. Instead of starting from a set of classical master equations, we begin with a low-level description of the underlying quantum mechanics, to ensure that we capture the physics we are looking for (as expected, the final result is equivalent to what one would get by starting with the classical description). We begin with a decomposition of the molecular state as a function of position in the cavity $\mathbf{r}$ and time t into two ro-vibrational states $|a\rangle$ and $|b\rangle$ with frequencies ω_a and ω_b

respectively, along with a set of electronic states $|i\rangle$ (frequencies ω_i) [40]:

$$|\Psi(\mathbf{r}, t)\rangle = c_a(\mathbf{r}, t)\, e^{-i\omega_a t}|a\rangle + c_b(\mathbf{r}, t)\, e^{-i\omega_b t}|b\rangle + \sum_i c_i(\mathbf{r}, t)\, e^{-i\omega_i t}|i\rangle \ . \tag{1}$$

The Hamiltonian in this basis is $\widehat{\mathcal{H}} = \widehat{\mathcal{H}}_0 + \widehat{\mathcal{H}}_I$, where

$$\widehat{\mathcal{H}}_0 = \hbar \left[\omega_a\, |a\rangle\langle a| + \omega_b\, |b\rangle\langle b| + \sum_i \omega_i\, |i\rangle\langle i| \right] \tag{2}$$

$$\begin{aligned}
\widehat{\mathcal{H}}_I = &- \sum_i \boldsymbol{\mathcal{E}}(\mathbf{r}, t) \cdot \boldsymbol{\mu}_{ai}\, |a\rangle\langle i| - \sum_i \boldsymbol{\mathcal{E}}(\mathbf{r}, t) \cdot \boldsymbol{\mu}_{bi}\, |b\rangle\langle i| \\
&- \sum_i \boldsymbol{\mathcal{E}}^*(\mathbf{r}, t) \cdot \boldsymbol{\mu}_{ai}^*\, |i\rangle\langle a| - \sum_i \boldsymbol{\mathcal{E}}^*(\mathbf{r}, t) \cdot \boldsymbol{\mu}_{bi}^*\, |i\rangle\langle b|
\end{aligned} \tag{3}$$

and where $\boldsymbol{\mathcal{E}}$ is the electric field vector and $\boldsymbol{\mu}_{xy}$ is the dipole moment between states $|x\rangle$ and $|y\rangle$. There are no direct transitions between states $|a\rangle$ and $|b\rangle$ (i.e., $\boldsymbol{\mu}_{ab} = \mathbf{0}$).

We decompose the electric field into cavity modes indexed by q (frequencies ω_q).

$$\boldsymbol{\mathcal{E}}(\mathbf{r}, t) = \frac{1}{2} \sum_q \left[\mathcal{E}_q(t)\, e^{-i\omega_q t}\, \mathbf{u}_q(\mathbf{r}) + \mathcal{E}_q^*(t)\, e^{i\omega_q t}\, \mathbf{u}_q^*(\mathbf{r}) \right] \ , \tag{4}$$

where $\mathbf{u}_q(\mathbf{r})$ is the mode shape function for mode q. We use lower-case subscripts for generic mode indices and upper-case color-coded subscripts for specific modes throughout. An energy level diagram for this system is shown in Fig. 2.
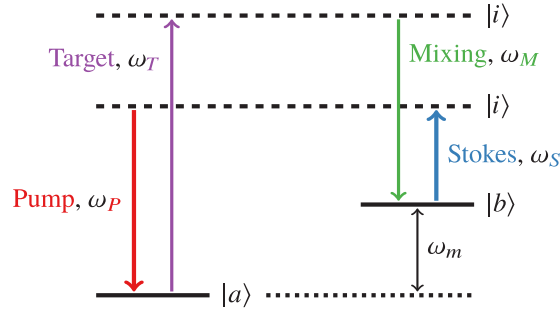

Fig. 2. The energy level diagram for molecular modulation. Two stable molecular rovibrational states $|a\rangle$ and $|b\rangle$ interact with four photons via two intermediate virtual states (both labeled $|i\rangle$). The Raman frequency shift ω_m is the frequency difference between the molecular states. The arrows are in the correct direction for term $MSP \to T$.

Armed with this decomposition, we eliminate the electronic states $|i\rangle$ from the evolution equations for $c_a(\mathbf{r}, t)$ and $c_b(\mathbf{r}, t)$, assume that the interaction is perturbative, and solve for the molecular polarization in terms of the $\mathcal{E}_q$. This polarization is inserted into the evolution equations for the $\mathcal{E}_q$ themselves, which include additional terms for the intrinsic decay of the mode energy as well as input power from launched beams coupled to the resonator [41,42]. After much simplification, we arrive at a final result that is similar in form to the sideband model:

$$\begin{aligned}
\dot{\mathcal{E}}_q(t) = &-\frac{\omega_q}{2Q_q} \mathcal{E}_q + \frac{1}{2}\sqrt{\frac{\omega_q}{Q_q^C E_q}} \sum_l \sqrt{S_l}\, e^{-i(\omega_q - \omega_l)t} \\
&+ i \sum_{r,s,t} G_{rstq}\, \omega_q\, \mathcal{E}_r\, \mathcal{E}_s^*\, \mathcal{E}_t\, \frac{V_{rstq}}{V_{qq}} \left(\frac{1}{\delta_{st}^*} + \frac{1}{\delta_{ts}} \right) e^{i\Delta_{rstq} t} \ ,
\end{aligned} \tag{5}$$

where q is the index of the cavity mode whose derivative we are evaluating, and r, s, and t are indices for a sum over all of the cavity modes (including mode q).

Each mode q has an intrinsic quality factor Q_q^I, which describes the decay of the mode's stored energy, and a coupling quality factor Q_q^C, which describes how easily light can move from it into the fiber or vice-versa. The total effective quality factor for each mode Q_q is given by $1/Q_q = 1/Q_q^I + 1/Q_q^C$. The first term of Eq. (5) thereby accounts for both the intrinsic decay of the mode energy and the power that couples out to the fiber.

The second term is the power that couples into the mode from the fiber. It keeps track of each launched beam l with frequency ω_l and power S_l independently. The factor E_q is the prefactor in the mode energy $U_q = E_q|\mathcal{E}_q|^2$.

The terms in the sum are the nonlinear four-wave mixing interaction, with a mode-dependent Raman gain coefficient G_{rstq}. Two volume factors appear; both are volume integrals of mode shapes $\mathbf{u}_q$ over the resonator volume, defined by

$$V_{abc\cdots} = \int d^3r |\mathbf{u}_a||\mathbf{u}_b||\mathbf{u}_c|\cdots .\qquad(6)$$

V_{rstq} is a four-mode shape overlap, and V_{qq} is simply the mode volume. Two frequency differences appear in these terms: the two-mode Raman detuning $\delta_{xy} = (\omega_x - \omega_y) - \omega_m + i\gamma_R$ (where γ_R is the Raman linewidth), and the four-mode detuning $\Delta_{rstq} = \omega_r - \omega_s + \omega_t - \omega_q$. For convenience, we consolidate the various prefactors of each term to get the following form:

$$\dot{\mathcal{E}}_q = -\mathcal{D}_q\,\mathcal{E}_q + \mathcal{P}_q \sum_l \sqrt{S_l}\,e^{-i(\omega_q-\omega_l)t} + i\sum_{r,s,t} \mathcal{G}_{rstq}\,\mathcal{E}_r\,\mathcal{E}_s^*\,\mathcal{E}_t\,e^{i\,\Delta_{rstq}\,t} .\qquad(7)$$

The primary differences between Eq. (7) and the sideband model are that we have not restricted the sum over possible four-wave mixing terms, and that we have allowed more than one launched beam. One can reduce Eq. (7) to the sideband model by restricting the sums appropriately, and we have confirmed that in that form the model reproduces expected behavior such as clamping during cascaded SRS [38], which we also see in the full model.

Even in the fully-general case, the most important terms in the sum for a given mode q can be identified in advance by a simple graphical algorithm using the energy level diagram in Fig. 2. We label the terms by the four modes they involve, so the term $i\,\mathcal{G}_{MSPT}\,\mathcal{E}_M\mathcal{E}_S^*\mathcal{E}_T\,\exp(i\,\Delta_{MSPT}\,t)$ is labeled $MSP \to T$. The notation indicates that this term is the one where modes M, S, and P contribute to the derivative of T.

The arrows on the diagram must form a closed loop (their directions may need to be reversed) to have small Δ_{rstq} (see Sec. 3.2), so important terms must be either of the form $qrr \to q$ (two pairs of modes) or $rst \to q$ (all four modes different). Additionally, arrows that do not touch the same energy level must not appear next to each other (e.g., T cannot appear next to S). Finally, the last mode's arrow must point upward (this corresponds to an arbitrary sign convention in the derivation and has no physical significance; if the sign choice were reversed, the term with the last arrow pointing downward would be the important one).

For example, the most relevant terms for the target mode T must be of the forms $Trr \to T$ or $rst \to T$. For the first form, rr could be either MM, PP, or SS. These correspond to the possibility of stimulated Raman scattering (SRS) between the target and mixing, pump, or Stokes modes. For the second form, the T arrow must point upward, so we are forced to go around the diagram in an order that gives us the term $MSP \to T$. This term corresponds to molecular modulation: it says that energy can be delivered to the target mode from the other three modes via four-wave mixing.

3. Computational modeling

We can make some predictions about the behavior of an MMM by simulating Eq. (7) numerically. In this section we will first lay out the assumptions behind our simulations, then discuss the dependence of the modulation efficiency ϵ on a variety of parameters.

We evolve the mode amplitudes in time using a simple Runge-Kutta scheme with a time step of a few picoseconds, which is enough to resolve frequency detunings of up to a few hundred GHz (more than large enough to resolve all of the important terms in Eq. (7)). For consistency, four-wave mixing terms in Eq. (7) that have a Δ_{qrst} larger than the Nyquist frequency for the chosen time step are not included in the calculation. The simulations are converged with respect to the time step and always reach a steady-state with constant energy in each mode. The final energies do not depend on the relative timing of the launched pump and mixing beams being turned on, so we turn both beams on at the beginning of the simulation.

We take the resonator to be a silica microsphere with radius $R = 50\,\mu$m. We model the silica Raman shift as a Lorentzian with $\omega_m = 2\pi \times 12$ THz and a linewidth of 2 THz, and the $\mathcal{G}_{rstq}$ are calculated from the bulk Raman coefficient [43]. We take the intrinsic quality factors of all of the modes to be 10^8 (quality factors this high have been regularly achieved in practice [36]), except in Sec. 3.4 where we look at how the modulation efficiency depends on it.

Light is coupled to and from the resonator using a tapered fiber. We generally either calculate the coupling quality factors from Eq. (35) of [44] with a 1 μm taper radius and the pump mode critically coupled to the launched pump beam ("pump-critical"), or we take all of the modes to be critically coupled ("all-critical"). The pump-critical case does not give the highest modulation efficiency, but it does have the lowest threshold (this will be addressed in Sec. 3.5).

The all-critical case is roughly equivalent to adding a second tapered fiber to the system, with coupling optimized for the mixing mode instead of the pump mode. This kind of coupling scheme is common for communications applications [45,46], and could be re-purposed for the MMM. It would be necessary to prevent the secondary fiber from disturbing the coupling between the first fiber and the microsphere, perhaps by suppressing any propagating fiber modes near that wavelength using an engineered stopband [47]. However, the purpose of this case is just to approximate the maximum possible theoretical efficiency of the system, and in our simulations we simply assume it might be possible without implementing a model of how it would work in practice. As we will see in Sec. 3.5, even this is not the most ideal coupling scheme.

For better control over the parameters of the simulation, we use representative modes instead of real cavity modes. The mode volumes and four-mode shape overlaps of the representative modes are given values calculated from averages over real cavity modes, while we set the modes frequencies and intrinsic quality factors arbitrarily. It is important to control the mode frequencies exactly because the modulation efficiency is quite sensitive to the four-mode detuning Δ_{rstq}, which is a measure of the timescale over which the modulation process conserves energy. We will generally set the four-mode detuning for the molecular modulation path to zero. A possible method for control of the four-mode detuning will be discussed in Sec. 3.2.

As mentioned above, the mode volumes V_{qq} and four-mode shape overlaps V_{rstq} are given uniform values for all modes that are representative of the average volumes and overlaps calculated from real cavity modes [36,48]. The actual mode volumes and four-mode shape overlaps vary up and down somewhat-independently from mode to mode over the range of mode wavelengths we use by approximately an order of magnitude, depending on the wavelengths of the modes, their angular momentum and radial quantization numbers, and their polarizations. Since the four-wave mixing terms in Eq. (5) depend only on the ratio between a four-mode overlap and a mode volume, we expect the real modulation efficiencies to be within an order of magnitude of those calculated with the representative values.

For simplicity, we assume that cascaded SRS has been suppressed. This could perhaps be achieved in practice [49], but actually turns out to be irrelevant. We have run the same simulations

with enough higher-order Stokes modes to capture the full cascade at the highest launched pump powers that we show below, and there is no significant difference in the modulation efficiency compared to simulations without the cascaded modes (this surprising result will be discussed in Sec. 3.1). The launched mixing power is always $S_M = 1\,\mu W$, which is below the threshold for the mixing mode to create its own Stokes mode.

Our simulations do not take into account other nonlinear processes, such as generation of parametric sidebands through self-phase modulation, which is due to the Kerr nonlinearity [50]. The Kerr and Raman nonlinearities are both third order, so one would expect their thresholds to be comparable. In a real experiment, there will likely be additional modes excited near the pump mode due to Kerr mixing. However, there is good reason to believe that the existence of these additional excited modes will not significantly change our results.

First, the primary effect of these modes will be to deplete the energy of the pump mode. However, in Raman lasing, the pump energy inside the resonator is clamped once it reaches the Stokes lasing threshold [38]. When a Raman laser is pumped far above threshold, a large fraction of the incident pump power does not couple into the resonator. This excess incident pump power can overcome any additional depletion of the pump beam due to the presence of other nonlinear optical processes. Second, the additional four-wave mixing pathways made available by these extra excitations will not, in general, produce a target frequency that is aligned with a resonator mode frequency (i.e., these terms will have large four-mode detunings). As we will see in Sec. 3.2, this should suppress any additional modulation of the mixing beam. However, a detailed analysis of all of these additional nonlinear processes in addition to Raman generation is beyond the scope of this work, and possibly too computationally expensive to explore with the mode-based simulations we use.

3.1. Dependence on launched pump power

An important metric for a modulator is the modulation efficiency ϵ, which we define to be the output power of the target mode P_T divided by the launched mixing power S_M ($\epsilon = P_T / S_M$). Since the molecular modulation process only relies on establishing coherence between the molecular states through SRS, we should only expect non-zero modulation efficiency as soon as the pump mode energy goes above the threshold to produce a Stokes mode. Figure 3 shows that this is indeed the case.

The modulation efficiency curves are quite unlike what we expected based on the behavior of our previous device. In that system the mixing and target frequencies were not resonant in the cavity, so the target light was produced in a single pass of the mixing beam through the system. The modulation efficiency was very low, so the pump mode, Stokes mode, and mixing beam were essentially unperturbed by the molecular modulation process. This allowed the modulation efficiency to scale roughly like the Stokes mode energy in the ideal case. In contrast, the situation in the MMM is shown in Fig. 4. The mixing mode energy decreases after an initial plateau, corresponding to the decrease in the modulation efficiency.

To investigate this counterintuitive decrease, we start by noting that the complex mixing mode amplitude $\mathcal{E}_M$ is constant at steady-state (not just the mode energy U_M) because it is externally pumped. Therefore, we can set the derivative of $\mathcal{E}_M$ to zero at steady-state, assume that it is too far detuned from the launched pump beam to interact with it, and write

$$\dot{\mathcal{E}}_M = 0 = -\mathcal{D}_M \mathcal{E}_M + \mathcal{P}_M \sqrt{S_M} + i \sum_{r,s,t} \mathcal{G}_{rstM}\, \mathcal{E}_r\, \mathcal{E}_s^*\, \mathcal{E}_t\, e^{i\,\Delta_{rstM}\, t} \tag{8}$$

$$\mathcal{E}_M = \frac{\mathcal{P}_M}{\mathcal{D}_M} \sqrt{S_M} + i \sum_{r,s,t} \frac{G_{rstM}}{\mathcal{D}_M}\, \mathcal{E}_r\, \mathcal{E}_s^*\, \mathcal{E}_t\, e^{i\,\Delta_{rstM}\, t}\,. \tag{9}$$

This equation does not let us determine $\mathcal{E}_M$ from the initial conditions, but it does let us explain why $\mathcal{E}_M$ has the steady-state value it does phenomenologically. The most important terms in
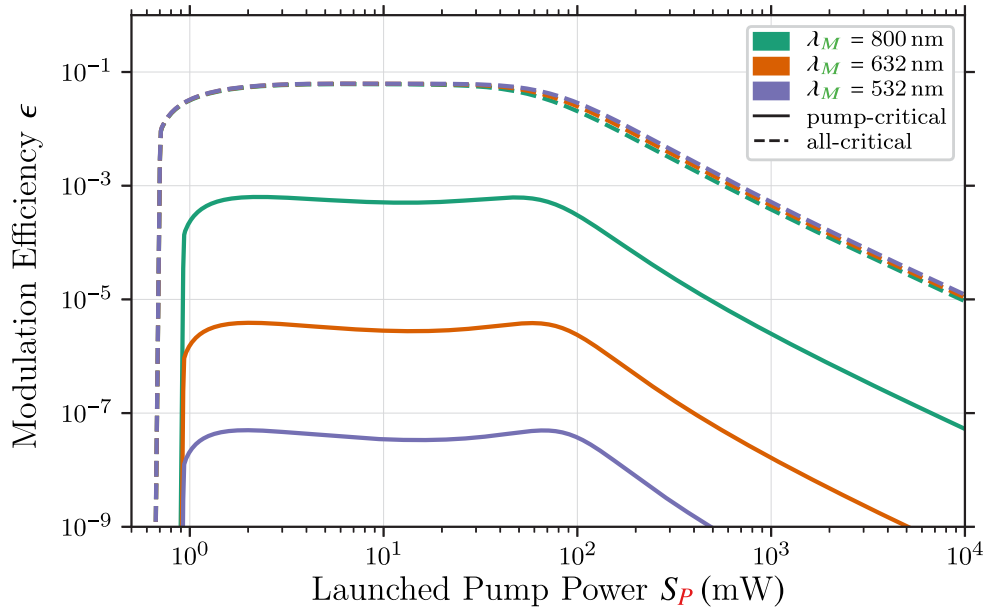
Fig. 3. The modulation efficiency ϵ as a function of launched pump power S_P for three different mixing wavelengths λ_M. The modulation efficiency is $\epsilon = P_T/S_M$, where P_T is the target mode output power and S_M is the launched mixing power. The pump mode wavelength is $\lambda_P = 1064$ nm, and it is critically coupled to the launched pump beam.
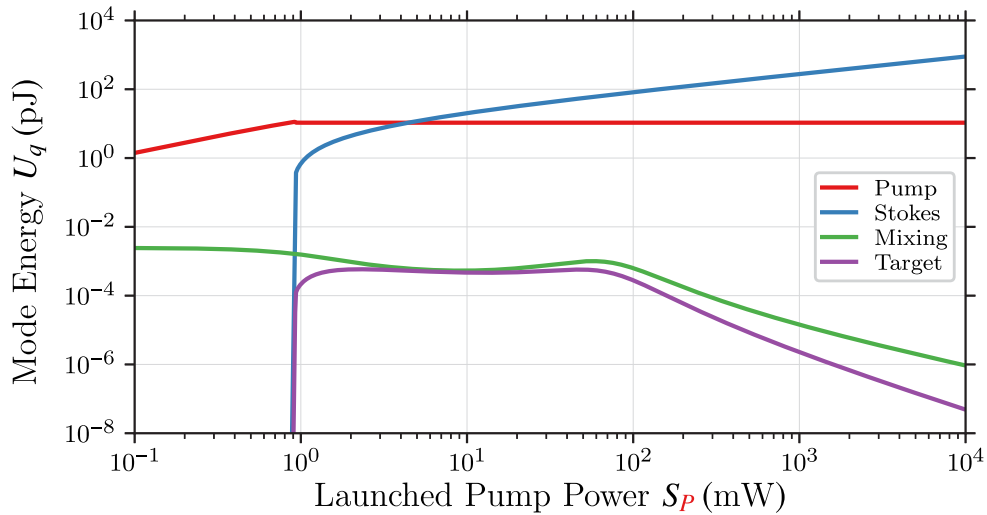

Fig. 4. The energy stored in each resonator mode U_q as a function of launched pump power S_P. After threshold, U_P is clamped and U_S grows like the square root of the launched pump power. After an initial plateau following threshold, U_M and U_T begin to decrease, which reduces the modulation efficiency.

Eq. (9) are shown in Fig. 5 for one of the curves from Fig. 3. Note that all of these terms have a four-mode detuning of zero in these simulations, so they do not have time-dependent phases that do not arise from the mode amplitudes themselves. As expected, the launched mixing beam and the four wave mixing are both important. However, another term is also important:

$MSS \rightarrow M$, which corresponds to SRS between the mixing mode and the Stokes modes (the next most important is $MPP \rightarrow M$, not shown).
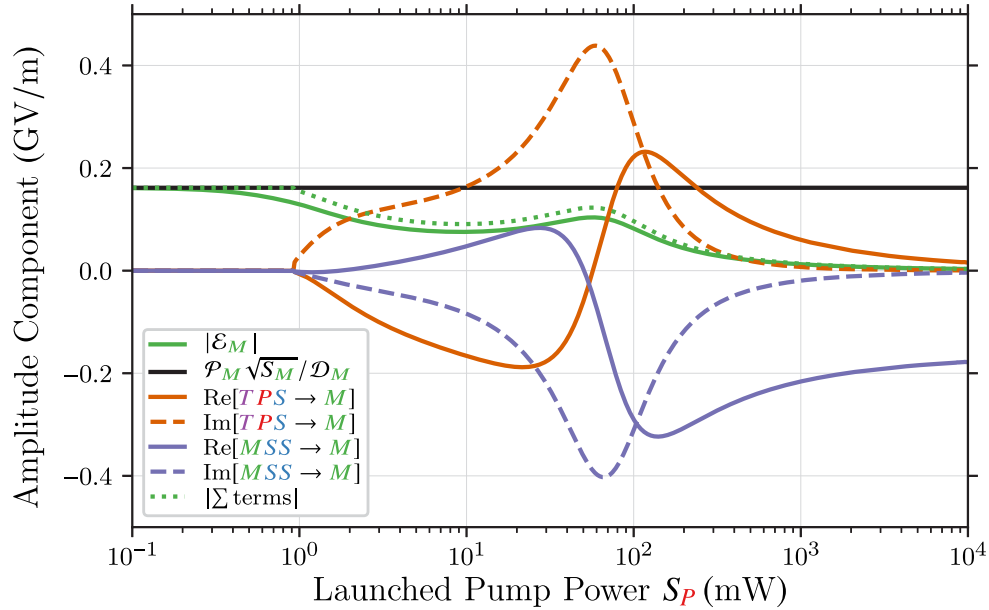

Fig. 5. The real and imaginary contributions of the three most important terms in Eq. (9) to the mixing mode amplitude (magnitude plotted as $|\mathcal{E}_M|$): the launched mixing beam, the molecular modulation term $TPS \rightarrow M$, and the SRS term $MSS \rightarrow M$. These three terms together almost entirely compose the steady-state mixing mode amplitude (the magnitude of their sum is plotted in dotted green).

SRS would normally be suppressed between these modes because they are not on Raman-resonance. However, the Raman linewidth of silica is several THz, so the frequency difference is not enough to suppress this term when the Stokes mode energy is large. Although the simulations we present here only include one Stokes mode, we have performed similar simulations with enough higher-order Stokes modes to model the entire cascade out to $S_P = 10$ W, and there is no significant difference in the behavior of the modulator. The combined effect of all of the cascaded Stokes modes together is similar to the single large un-cascaded Stokes mode. This effect is why there is no significant difference in modulation efficiency between simulations run with and without cascaded Stokes modes.

Remarkably, this off-resonant SRS actually supports the mixing mode, causing the plateau. We ran a set of simulations with the Raman linewidth reduced by a factor of 10^3 (i.e., it is a few GHz instead of a few THz) while keeping everything else constant. This suppresses the off-resonant SRS between the mixing mode and pump or Stokes modes. The mode energies and mixing mode amplitude composition for these simulations are shown in the left and right panels of Fig. 6 respectively. With no SRS from the mixing mode to the pump or Stokes modes, the mixing and target mode energies begin to decrease immediately after threshold with no plateau. Now the only important terms in the mixing mode amplitude are the external beam and the molecular modulation term, as originally expected.

Now that the off-resonant SRS has been suppressed, all four modes have nearly-constant complex amplitude at steady state. If we approximate them as constant, we can solve for the amplitudes of the target and mixing modes in terms of the pump and Stokes mode amplitudes. Using the graphical algorithm for determining relevant terms described above, we can solve for
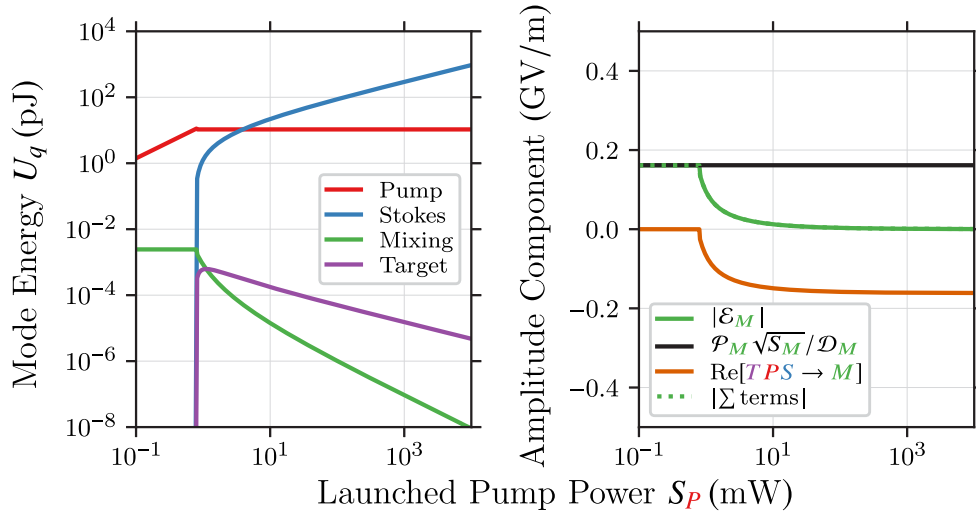
Fig. 6. Mode energies (left) and mixing mode amplitude composition (right) when the Raman linewidth has been artificially reduced by a factor of 10^3. The mixing and target mode energies now drop off without a plateau. There are only two important contributions to the mixing mode amplitude: the launched mixing beam and the molecular modulation term $TPS \rightarrow M$ (which is now purely real). These two terms together entirely compose the mixing mode amplitude at steady-state (the two green curves overlap). The reduction of the Raman linewidth has removed the off-resonant SRS between the mixing mode and other modes that was present in Fig. 5.

the target mode amplitude:

$$\dot{\mathcal{E}}_T = 0 = -\mathcal{D}_T \mathcal{E}_T + i\,\mathcal{G}_{MSPT}\,\mathcal{E}_M\,\mathcal{E}_S^*\,\mathcal{E}_P \tag{10}$$

$$\mathcal{E}_T = i\,\frac{\mathcal{G}_{MSPT}}{\mathcal{D}_T}\,\mathcal{E}_M\,\mathcal{E}_S^*\,\mathcal{E}_P\,. \tag{11}$$

We can use Eq. (11) to solve for $\mathcal{E}_M$, arriving at a form that only depends on $\mathcal{E}_P$ and $\mathcal{E}_S$:

$$\dot{\mathcal{E}}_M = 0 = -\mathcal{D}_M \mathcal{E}_M + \mathcal{P}_M \sqrt{S_M} + i\,\mathcal{G}_{TPSM}\,\mathcal{E}_T\,\mathcal{E}_P^*\,\mathcal{E}_S \tag{12}$$

$$0 = -\mathcal{D}_M \mathcal{E}_M + \mathcal{P}_M \sqrt{S_M} + i^2\,\mathcal{G}_{TPSM}\,\frac{\mathcal{G}_{MSPT}}{\mathcal{D}_T}\,\mathcal{E}_M\,\mathcal{E}_S^*\,\mathcal{E}_P\,\mathcal{E}_P^*\,\mathcal{E}_S \tag{13}$$

$$\mathcal{E}_M = \frac{\mathcal{P}_M \sqrt{S_M}}{\mathcal{D}_M + \mathcal{G}_{TPSM}\,\mathcal{G}_{MSPT}\,|\mathcal{E}_P|^2\,|\mathcal{E}_S|^2/\mathcal{D}_T}\,. \tag{14}$$

When $|\mathcal{E}_S|^2$, which is proportional to the Stokes mode energy, becomes large, the second term in the denominator dominates the first and $\mathcal{E}_M$ begins to decrease. This is the root cause of the decrease in modulation efficiency: the mixing mode amplitude decreases like $|\mathcal{E}_S|^2$, which causes the target mode amplitude to go like $\mathcal{E}_T \sim \mathcal{E}_M\,\mathcal{E}_S^* \sim \mathcal{E}_S^*/|\mathcal{E}_S|^2 \sim 1/\mathcal{E}_S$ (from Eq. (11)).

This behavior is similar to pump mode clamping in cascaded SRS, where the behavior of a mode that is not being externally pumped causes a change in the form of the evolution equation for another mode that changes its qualitative dynamics. The off-resonant SRS terms, despite their apparently-detrimental behavior in Fig. 5, provide extra paths for energy flow that limit the effect of the clamping-like behavior described by Eq. (14) until the Stokes mode reaches much higher energy. This causes the plateau that we observe in the modulation efficiency in Fig. 3. An

observer in the lab would see the launched mixing beam have higher transmission through the fiber as the launched pump power increases, much like the launched pump beam itself begins to have higher transmission due to traditional SRS clamping.

Although this clamping-like effect prevents the modulation efficiency from scaling like the Stokes amplitude as we initially expected, the modulation efficiencies in the plateau region are still very high. Even the simple single-fiber coupling setup gives an efficiency of approximately 0.1% at $\lambda_M = 800$ nm, several orders of magnitude higher than our previous modulator. Critical coupling could boost the efficiency to nearly 10%. The existence of the plateau means that the modulation efficiency should be quite stable to fluctuations in the launched pump power. The MMM will also never need much more launched pump power than the threshold power.

3.2. Dependence on four-mode detuning

Bringing the four-mode detuning Δ_{MSPT} down to less than a mode linewidth $\Gamma_q = \omega_q/Q_q$ (a few MHz for optical frequencies if $Q_q \approx 10^8$) is necessary for high-efficiency operation. Figure 7 shows what happens when Δ_{MSPT} (which is equal to the target mode detuning δ_T in that figure) becomes larger than the target mode linewidth Γ_T. As Δ_{MSPT} grows, the exponential phase in the relevant terms in Eq. (7) becomes too fast to effectively drive the target mode, and the target mode energy (and therefore output power) begins to decrease like $1/(\Delta_{MSPT}/\Gamma_T)^2$. Equivalently, when this process fails to conserve energy (i.e., when $\hbar\Delta_{MSPT}$ is non-zero), the steady-state efficiency decreases. However, as long as $\Delta_{MSPT} < \Gamma_T$, there is no significant change in ϵ from perfect four-mode resonance.
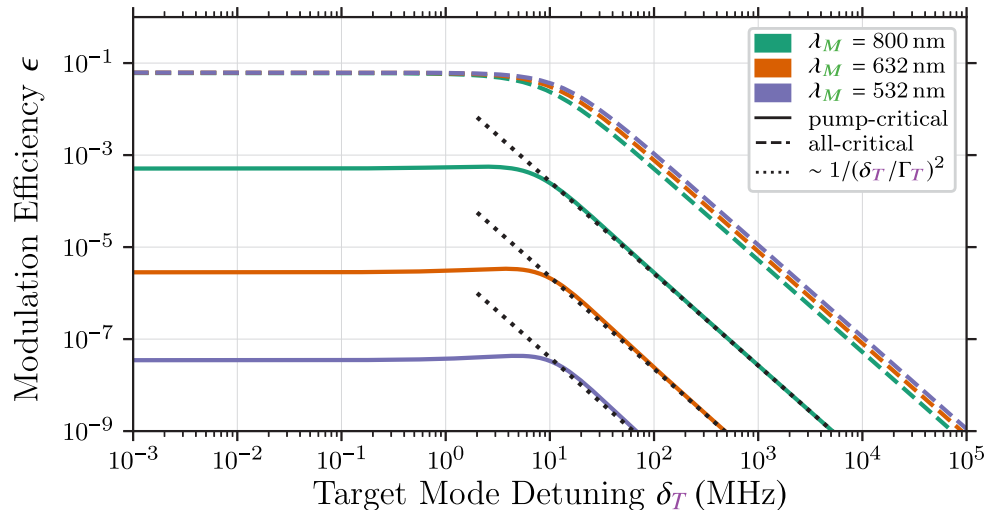

Fig. 7. The modulation efficiency as the target mode frequency ω_T is detuned from perfect four-mode resonance. Since the other mode frequencies are constant, $\delta_T = \Delta_{MSPT}$, which appears in the molecular modulation terms in Eq. (7). As the detuning becomes larger than the target mode linewidth Γ_T (a few MHz for each λ_M), the modulation efficiency begins to decrease.

Because the mode structure in a microresonator is generally quite irregular, it is important to consider how we could achieve low four-mode detuning in an actual device. One possible method is that the resonator's mode frequencies could be tuned via the material's thermo-optic response (the change in index of refraction $n(\omega, T)$ with temperature T). The first-order thermo-optic coefficient in silica is $\alpha_n = 1.09 \times 10^{-5}$ K^{-1} [51]. For small changes in the index of refraction, the resonator's mode frequencies will change by the same fraction that the index of refraction at

that frequency changes [36]:

$$\frac{\partial \omega}{\partial T} \approx \frac{\omega}{n(\omega, T)} \frac{\partial n(\omega, T)}{\partial T} = \frac{\omega}{n(\omega, T)} \alpha_n .$$

(15)

Thus we have

$$\frac{\partial \Delta_{MSPT}}{\partial T} \approx \alpha_n \left(\frac{\omega_M}{n(\omega_M, T)} - \frac{\omega_S}{n(\omega_S, T)} + \frac{\omega_P}{n(\omega_P, T)} - \frac{\omega_T}{n(\omega_T, T)} \right) .$$

(16)

If we use $\lambda_P = 1064$ nm and $\lambda_M = 800$ nm, assume that $\omega_T \approx \omega_M + 2\pi \times 12$ THz and $\omega_S \approx \omega_P - 2\pi \times 12$ THz, and use the Sellmeier coefficients for silica at 20 °C [52], we find that $\frac{\partial \Delta_{MSPT}}{\partial T} \approx 2.0$ MHz K^{-1}. With $\lambda_M = 532$ nm, $\frac{\partial \Delta_{MSPT}}{\partial T} = 9.1$ MHz K^{-1}.

This calculation indicates that the four-mode detuning could be adjusted by at least a few tens of MHz by a standard thermoelectric controller for any mixing wavelength in the optical region of the spectrum. Although the free spectral range in microresonators is generally at least a few GHz, the actual mode spacing (i.e., the distance to the mode with the closest frequency, not the next mode in the same family) in a non-ideal device can be much denser. For example, by giving a spherical microresonator a small eccentricity to lift the degeneracy of the whispering gallery modes, the actual spacing between adjacent modes could be reduced to a few tens of MHz [53], meaning the four-mode detuning should never be off by more than a few tens of MHz to begin with. However, one may still need to try many different four-mode sets to find a set with high modulation efficiency (due to the mode-dependent coupling factors).

3.3. Dependence on mixing wavelength

One of the key advantages of the MMM is that, depending on the size, geometry, and material of the microresonator, modes could be available over a wide range of wavelengths. Figure 8 shows how the modulation efficiency varies with the wavelength of the mixing mode. From the left panel we see that in the pump-critical case the modulation efficiency decreases dramatically
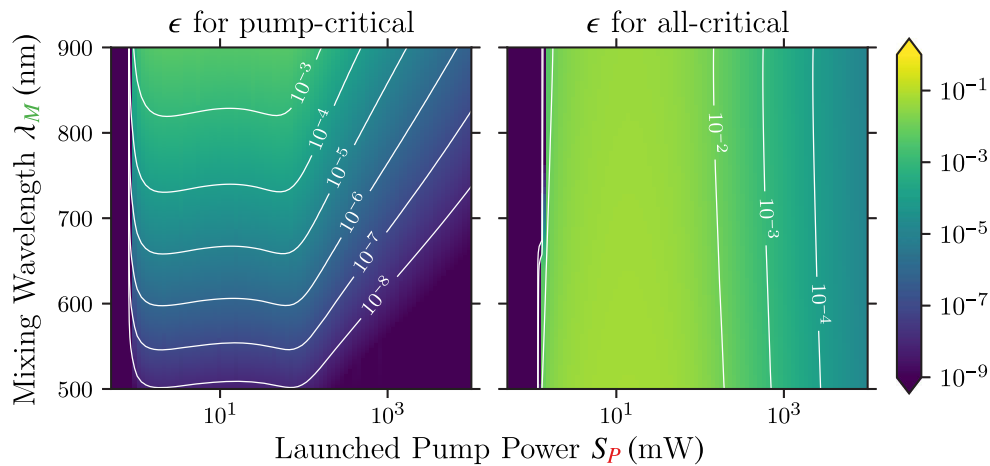

Fig. 8. The modulation efficiency $\epsilon = P_T/S_M$ as a function of the launched pump power S_P and the mixing mode wavelength λ_M, with the pump mode critically coupled (left) or all modes critically coupled (right). The dominant factor in the decreasing modulation efficiency on the left is the increasingly-non-critical coupling between the fiber and the mixing mode as λ_M is moved further from the pump wavelength $\lambda_P = 1064$ nm. On the right, where all modes are critically coupled, ϵ is essentially independent of λ_M.

as the separation between the pump and mixing wavelengths increases because the mixing and target modes become poorly coupled to the fiber (i.e., Q_M^I is not close to Q_M^C). However, if we can critically couple all of the modes, ϵ becomes largely independent of λ_M throughout the optical spectrum, as illustrated in the right panel.

In reality, we would still expect some variation with λ_M because the mixing and target mode volumes and four-mode overlaps will vary, as discussed earlier. Nevertheless, as long as the MMM is built with the capability to adjust the coupling scheme and resonator temperature appropriately, the same device should be able to modulate efficiently over a large, continuous range of mixing beam wavelengths.

3.4. Dependence on intrinsic quality factor

Another factor that we could control is the intrinsic quality factor of the microsphere. So far, we have assumed that it is fixed at $Q^I = 10^8$. However, microspheres could be produced with either smaller or larger intrinsic quality factors than that. The results of simulations where we vary the intrinsic quality factor are shown in Fig. 9.
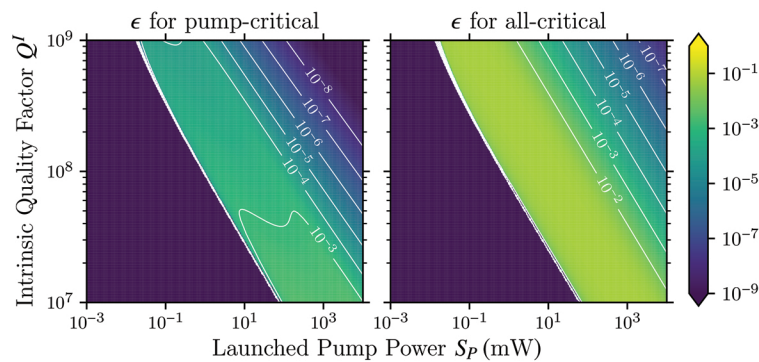

Fig. 9. The modulation efficiency $\epsilon = P_T/S_M$ as a function of the launched pump power S_P and the intrinsic quality factor Q^I, with the pump mode critically coupled (left) or all modes critically coupled (right). The pump and mixing wavelengths are $\lambda_P = 1064$ nm and $\lambda_M = 800$ nm. When the intrinsic quality factor increases, threshold is decreased, but modulation efficiency also decreases, and vice-versa.

When the intrinsic quality factor is increased at fixed launched pump power the modulation efficiency decreases. Increasing the intrinsic quality factor is essentially the same as shifting the curves in Fig. 3 to lower pump power: threshold decreases, but since we are at fixed launched pump power, we are now further out on the curve, where we already know the modulation efficiency begins to decrease.

3.5. Dependence on fiber separation

So far, we have been working with two coupling schemes: either there is a single fiber critically coupled to the pump mode, or all of the modes are critically coupled. In this section, we will use a single fiber as in the first case, but we will change its distance from the microsphere (the fiber separation s). As s decreases, the coupling quality factor Q^C decreases at all wavelengths, meaning that light can more easily move between the fiber and the microsphere. This scheme is the easiest to achieve experimentally, requiring no special modifications of the fiber or microsphere.

The results, shown in Fig. 10, show that the modulation efficiency tends to increase as Q^C decreases, with no special behavior near the critical separations. This is a result of the target mode not being directly pumped: we do not need to balance input and output power to get critical

coupling, we just need to maximize the output power. Decreasing Q^C lets more light leave the target mode and go to the fiber. Simultaneously, the threshold pump power is increasing, but this is not necessarily detrimental, because we know from Sec. 3.1 that there is no reason to go far beyond threshold. So we have an indirect route to increasing the modulation efficiency by increasing the launched pump power (which eluded us in Sec. 3.1): if we have spare pump power, we can move the fiber closer to the microsphere to get higher efficiency.
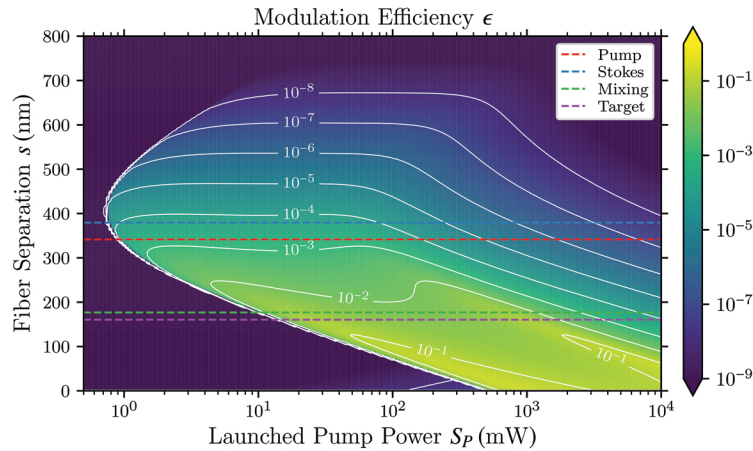

Fig. 10. The modulation efficiency $\epsilon = P_T/S_M$ as a function of the launched pump power S_P and the fiber separation s. Horizontal dashed lines are the fiber separations where each mode is critically coupled (but note that there is no special behavior at these separations). The pump and mixing wavelengths are $\lambda_P = 1064$ nm and $\lambda_M = 800$ nm, and the fiber taper radius is 1 μm. The coupling quality factors Q_q^C decrease for all modes as the fiber separation decreases.

These results also indicate that the all-critical coupling scheme is not the coupling scheme that maximizes the modulation efficiency. Determining the ideal scheme will depend on a variety of other design parameters and will involve a detailed search through the coupling and intrinsic quality factor parameter space for each mode (in addition to determining how to achieve those quality factors in practice). We plan to explore this in future work.

4. Conclusions

Optical modulators with a modulation frequency of ~ 10 THz and an efficiency exceeding 1% will have important applications in a number of research areas. For example, an MMM could be used to produce coherent light at currently-inaccessible parts of the spectrum, such as in the THz regime. An infrared mixing beam could be frequency-downshifted to efficiently produce THz radiation [54]. Another application is to optical waveform synthesis. Because the modulation efficiency is very large, higher-order Stokes and anti-Stokes sidebands could be produced by sending a mixing beam through several MMMs in series. These sidebands would form a broad spectrum, which could then be used to synthesize optical waveforms at femtosecond time scales.

Microsphere-based molecular modulators could represent a major step toward realizing these applications because they can potentially achieve extremely high modulation efficiency over a wide range of mixing beam wavelengths. Compared to our previous modulator, they also require less pump power, are more stable, are easier to operate, and are readily interoperable with other fiber-coupled devices.

There are still many challenges to overcome to build a functioning MMM: determining the optimal geometry and material for the microresonator, finding the best coupling scheme,

characterizing the time-dependent behavior during device startup, and understanding how the presence of additional excited modes and even intermode coupling will impact the modulation efficiency [38], to name just a few. Nevertheless, MMMs are a significantly better platform to work with than our previous modulator design, with a much higher ceiling for performance and a much lower floor for technical problems.

Funding

Acknowledgments

References

1. M. Chaciński, U. Westergren, B. Stoltz, L. Thylén, R. Schatz, and S. Hammerfeldt, "Monolithically Integrated 100 GHz DFB-TWEAM," J. Lightwave Technol. **27**(16), 3410–3415 (2009).
2. G. T. Reed, G. Mashanovich, F. Y. Gardes, and D. J. Thomson, "Silicon optical modulators," Nat. Photonics **4**(8), 518–526 (2010).
3. C. T. Phare, Y. H. Daniel Lee, J. Cardenas, and M. Lipson, "Graphene electro-optic modulator with 30 GHz bandwidth," Nat. Photonics **9**(8), 511–514 (2015).
4. Y. Enami, A. Seki, S. Masuda, T. Joichi, J. Luo, and A. K.-Y. Jen, "Bandwidth Optimization for Mach-Zehnder Polymer/Sol-Gel Modulators," J. Lightwave Technol. **36**(18), 4181–4189 (2018).
5. M. R. Javid, M. Miri, and A. Zarifkar, "Design of a compact high-speed optical modulator based on a hybrid plasmonic nanobeam cavity," Opt. Commun. **410**, 652–659 (2018).
6. J. K. Brasseur, K. S. Repasky, and J. L. Carlsten, "Continuous-wave Raman laser in H_2," Opt. Lett. **23**(5), 367 (1998).
7. J. K. Brasseur, P. A. Roos, K. S. Repasky, and J. L. Carlsten, "Characterization of a continuous-wave Raman laser in H_2," J. Opt. Soc. Am. B **16**(8), 1305 (1999).
8. K. Ihara, C. Eshima, S. I. Zaitsu, S. Kamitomo, K. Shinzen, Y. Hirakawa, and T. Imasaka, "Molecular-optic modulator," Appl. Phys. Lett. **88**(7), 074101 (2006).
9. S.-i. Zaitsu, C. Eshima, K. Ihara, and T. Imasaka, "Generation of a continuous-wave pulse train at a repetition rate of 176THz," J. Opt. Soc. Am. B **24**(5), 1037 (2007).
10. J. T. Green, D. E. Sikes, and D. D. Yavuz, "Continuous-wave high-power rotational Raman generation in molecular deuterium," Opt. Lett. **34**(17), 2563 (2009).
11. J. T. Green, J. J. Weber, and D. D. Yavuz, "Continuous-wave light modulation at molecular frequencies," Phys. Rev. A **82**(1), 011805 (2010).
12. J. T. Green, J. J. Weber, and D. D. Yavuz, "Continuous-wave, multiple-order rotational Raman generation in molecular deuterium," Opt. Lett. **36**(6), 897 (2011).
13. J. J. Weber, J. T. Green, and D. D. Yavuz, "17 THz continuous-wave optical modulator," Phys. Rev. A **85**(1), 013805 (2012).
14. D. C. Gold, J. J. Weber, and D. D. Yavuz, "Continuous-Wave Molecular Modulation Using a High-Finesse Cavity," Appl. Sci. **4**(4), 498–514 (2014).
15. D. C. Gold, J. T. Karpel, E. A. Mueller, and D. D. Yavuz, "Continuous-wave modulation of a femtosecond oscillator using coherent molecules," Opt. Lett. **43**(5), 1003 (2018).
16. A. E. Kaplan, "Subfemtosecond Pulses in Mode-Locked 2π Solitons of the Cascade Stimulated Raman Scattering," Phys. Rev. Lett. **73**(9), 1243–1246 (1994).
17. S. E. Harris and A. V. Sokolov, "Broadband spectral generation with refractive index control," Phys. Rev. A **55**(6), R4019–R4022 (1997).
18. S. E. Harris and A. V. Sokolov, "Subfemtosecond Pulse Generation by Molecular Modulation," Phys. Rev. Lett. **81**(14), 2894–2897 (1998).
19. H. Kawano, Y. Hirakawa, and T. Imasaka, "Generation of more than 40 rotational Raman lines by picosecond and femtosecond Ti:sapphire laser for Fourier synthesis," Appl. Phys. B: Lasers Opt. **65**(1), 1–4 (1997).
20. H. Kawano, Y. Hirakawa, and T. Imasaka, "Generation of high-order rotational lines in hydrogen by four-wave raman mixing in the femtosecond regime," IEEE J. Quantum Electron. **34**(2), 260–268 (1998).
21. A. V. Sokolov, D. R. Walker, D. D. Yavuz, G. Y. Yin, and S. E. Harris, "Raman generation by phased and antiphased molecular states," Phys. Rev. Lett. **85**(3), 562–565 (2000).
22. J. Q. Liang, M. Katsuragawa, F. L. Kien, and K. Hakuta, "Sideband Generation Using Strongly Driven Raman Coherence in Solid Hydrogen," Phys. Rev. Lett. **85**(12), 2474–2477 (2000).

23. M. Katsuragawa, J. Q. Liang, F. L. Kien, and K. Hakuta, "Efficient frequency conversion of incoherent fluorescent light," Phys. Rev. A **65**(2), 025801 (2002).
24. M. Y. Shverdin, D. R. Walker, D. D. Yavuz, G. Y. Yin, and S. E. Harris, "Generation of a Single-Cycle Optical Pulse," Phys. Rev. Lett. **94**(3), 033904 (2005).
25. W. J. Chen, Z. M. Hsieh, S. W. Huang, H. Y. Su, C. J. Lai, T. T. Tang, C. H. Lin, C. K. Lee, R. P. Pan, C. L. Pan, and A. H. Kung, "Sub-single-cycle optical pulse train with constant carrier envelope phase," Phys. Rev. Lett. **100**(16), 163906 (2008).
26. K. Wang, A. Zhdanova, M. Zhi, X. Hua, and A. Sokolov, "Multicolored Femtosecond Pulse Synthesis Using Coherent Raman Sidebands in a Reflection Scheme," Appl. Sci. **5**(2), 145–156 (2015).
27. C. Ohae, J. Zheng, K. Ito, M. Suzuki, K. Minoshima, and M. Katsuragawa, "Tailored Raman-resonant four-wave-mixing processes," Opt. Express **26**(2), 1452 (2018).
28. D. D. Yavuz, "High-frequency modulation of continuous-wave laser beams by maximally coherent molecules," Phys. Rev. A **76**(1), 011805 (2007).
29. A. B. Matsko and V. S. Ilchenko, "Optical resonators with whispering-gallery modes - Part I: Basics," IEEE J. Sel. Top. Quantum Electron. **12**(1), 3–14 (2006).
30. V. S. Ilchenko and A. B. Matsko, "Optical resonators with whispering-gallery modes - Part II: Applications," IEEE J. Sel. Top. Quantum Electron. **12**(1), 15–32 (2006).
31. I. S. Grudinin and L. Maleki, "Ultralow-threshold Raman lasing with CaF_2 resonators," Opt. Lett. **32**(2), 166 (2007).
32. I. S. Grudinin and L. Maleki, "Efficient Raman laser based on a CaF_2 resonator," J. Opt. Soc. Am. B **25**(4), 594–598 (2008).
33. P. Del'Haye, O. Arcizet, A. Schliesser, R. Holzwarth, and T. J. Kippenberg, "Full stabilization of a microresonator-based optical frequency comb," Phys. Rev. Lett. **101**(5), 053903 (2008).
34. T. Kato, A. Hori, R. Suzuki, S. Fujii, T. Kobatake, and T. Tanabe, "Transverse mode interaction via stimulated Raman scattering comb in a silica microcavity," Opt. Express **25**(2), 857 (2017).
35. T. Herr, V. Brasch, J. D. Jost, C. Y. Wang, N. M. Kondratiev, M. L. Gorodetsky, and T. J. Kippenberg, "Temporal solitons in optical microresonators," Nat. Photonics **8**(2), 145–152 (2014).
36. G. C. Righini, Y. Dumeige, P. Féron, M. Ferrari, G. N. Conti, D. Ristic, and S. Soria, "Whispering Gallery Mode microresonators: Fundamentals and applications," Riv. del Nuovo Cim. **34**, 435–488 (2011).
37. B. Min, T. J. Kippenberg, and K. J. Vahala, "Compact, fiber-compatible, cascaded Raman laser," Opt. Lett. **28**(17), 1507–1509 (2003).
38. T. J. Kippenberg, S. M. Spillane, B. Min, and K. J. Vahala, "Theoretical and experimental study of stimulated and cascaded Raman scattering in ultrahigh-Q optical microcavities," IEEE J. Sel. Top. Quantum Electron. **10**(5), 1219–1228 (2004).
39. K. S. Repasky, J. K. Brasseur, L. Meng, and J. L. Carlsten, "Performance and design of an off-resonant continuous-wave Raman laser," J. Opt. Soc. Am. B **15**(6), 1667 (1998).
40. J. J. Weber, "Continuous-Wave Light Modulation Using Stimulated Raman Scattering," Ph.D. thesis, University of Wisconsin-Madison (2014).
41. H. A. Haus, *Waves and Fields in Optoelectronics* (Prentice-Hall, 1984).
42. R. W. Boyd, *Nonlinear Optics* (Academic Press, 2008), 3rd ed.
43. D. Hollenbeck and C. D. Cantrell, "Multiple-vibrational-mode model for fiber-optic Raman gain spectrum and response function," J. Opt. Soc. Am. B **19**(12), 2886–2892 (2002).
44. M. L. Gorodetsky and V. S. Ilchenko, "Optical microsphere resonators: optimal coupling to high-Q whispering-gallery modes," J. Opt. Soc. Am. B **16**(1), 147–154 (1999).
45. M. Cai, G. Hunziker, and K. Vahala, "Fiber-optic add-drop device based on a silica microsphere-whispering gallery mode system," IEEE Photonics Technol. Lett. **11**(6), 686–687 (1999).
46. Y. Dong, K. Wang, and X. Jin, "Package of a dual-tapered-fiber coupled microsphere resonator with high Q factor," Opt. Commun. **350**, 230–234 (2015).
47. M. Sadgrove, R. Yalla, K. P. Nayak, and K. Hakuta, "Photonic crystal nanofiber using an external grating," Opt. Lett. **38**(14), 2542 (2013).
48. S. Balac, "WGMode: A Matlab toolbox for whispering gallery modes volume computation in spherical optical micro-resonators," Comput. Phys. Commun. **243**, 121–134 (2019).
49. A. Lee, H. M. Pask, and D. J. Spence, "Control of cascading in multiple-order Raman lasers," Opt. Lett. **37**(18), 3840 (2012).
50. S. M. Spillane, T. J. Kippenberg, and K. J. Vahala, "Ultralow-threshold Raman laser using a spherical dielectric microcavity," Nature **415**(6872), 621–623 (2002).
51. H. Gao, Y. Jiang, Y. Cui, L. Zhang, J. Jia, and L. Jiang, "Investigation on the thermo-optic coefficient of silica fiber within a wide temperature range," J. Lightwave Technol. **36**(24), 5881–5886 (2018).
52. I. H. Malitson, "Interspecimen Comparison of the Refractive Index of Fused Silica," J. Opt. Soc. Am. **55**(10), 1205 (1965).
53. K. Gardner, Y. Zhi, L. Tan, S. Lane, Y.-F. Xiao, and A. Meldrum, "Whispering gallery mode structure in polymer-coated lasing microspheres," J. Opt. Soc. Am. B **34**(10), 2140 (2017).
54. D. D. Yavuz and J. J. Weber, "Tunable source of terahertz radiation using molecular modulation," Opt. Lett. **37**(20), 4191 (2012).